nature communications

Article

https://doi.org/10.1038/s41467-024-53713-4

Metal chalcogenide electron extraction layers for *nip*-type tin-based perovskite solar cells

Received: 22 May 2024

Accepted: 18 October 2024

Published online: 01 November 2024

Check for updates

Tianpeng Li[1,6], Bin Li[2,6], Yingguo Yang[3,4], Zuoming Jin[1], Zhiguo Zhang[1], Peilin Wang[1], Liangliang Deng[5], Yiqiang Zhan[5], Qinghong Zhang[2] & Jia Liang[1]

Tin-based perovskite solar cells have garnered attention for their biocompatibility, narrow bandgap, and long thermal carrier lifetime. However, *nip*-type tin-based perovskite solar cells have underperformed largely due to the indiscriminate use of metal oxide electron transport layers originally designed for *nip*-type lead-based perovskite solar cells. Here, we reveal that this underperformance is caused by oxygen vacancies and deeper energy levels in metal oxide. To address these issues, we propose a metal chalcogenide electron transport layer, specifically $Sn(S_{0.92}Se_{0.08})_2$, which circumvents the oxygen molecules desorption and impedes the Sn^{2+} oxidation. As a result, tin-based perovskite solar cells with $Sn(S_{0.92}Se_{0.08})_2$ demonstrate a V_{OC} increase from 0.48 – 0.73 V and a power conversion efficiency boost from 6.98 – 11.78%. Additionally, these cells exhibit improved stability, retaining over 95% of their initial efficiency after 1632 h. Our findings showcase metal chalcogenides as promising candidates for future *nip*-type tin-based perovskite solar cell applications.

Organic-inorganic metal halide perovskite solar cells (PSCs) have attracted attention as a result of the meteoric rise in their power conversion efficiencies (PCEs) over the past several years[1–7]. In particular, lead (Pb)-based perovskites, including methylammonium lead iodide ($CH_3NH_3PbI_3$, $MAPbI_3$), formamidinium lead iodide ($CH(NH_2)_2PbI_3$, $FAPbI_3$), and their mixtures, were considered as highly attractive solar light-harvesting materials because of their high absorption coefficient, adjustable optical bandgap, high charge carrier mobility, and simple solution processing[8–17]. However, the toxicity of Pb to human beings and the environment cannot be ignored, which significantly hinders the future commercialization of Pb-based PSCs[18–22]. Therefore, considerable efforts have been made to explore environmentally friendly less-toxic or nontoxic perovskite materials to replace Pb, such as tin (Sn)[23–25], germanium (Ge)[26,27], bismuth (Bi)[28,29], and antimony (Sb)[30,31]. Among these candidates, tin-based PSCs (TPSCs) are recognized as the promising Pb alternative for several reasons. First, TPSCs possess a higher theoretical PCE than LPSCs according to the Shockley-Queisser (S-Q) limit[32–39]. Second, the most promising path toward the commercialization of PSCs involves developing all-perovskite tandem solar cells, which require narrow bandgap perovskites[40–48]. Tin-based and tin-lead-mixed perovskites are promising candidates for these narrow-bandgap perovskite materials. Finally, to date, TPSCs have achieved the highest PCE, exceeding 15%, among all Pb-free PSCs[32,36,49–58].

[1]Department of Materials Science and State Key Laboratory of Photovoltaic Science and Technology, Fudan University, 220 Handan Road, Shanghai 200433, China. [2]State Key Laboratory for Modification of Chemical Fibers and Polymer Materials, College of Materials Science and Engineering, Donghua University, Shanghai 201620, China. [3]School of Microelectronics, Fudan University, 220 Handan Road, Shanghai 200433, China. [4]Shanghai Synchrotron Radiation Facility (SSRF), Shanghai Advanced Research Institute, Chinese Academy of Sciences, Shanghai 201800, China. [5]Center of Micro-Nano System, School of Information Science and Technology, Fudan University, 220 Handan Road, Shanghai 200433, China. [6]These authors contributed equally: Tianpeng Li, Bin Li. e-mail: jialiang@fudan.edu.cn

Similar to the lead-based PSCs (LPSCs), TPSCs can also be classified into two architecture types, *nip* and *pin*, where the difference is defined by the order of deposition of the electron and hole transport layers relative to the transparent conductive oxide (TCO) substrate[32–38,40]. The highest performing TPSCs are currently achieved in the *pin* architecture[32,36]. However, *nip*-type TPSCs are also of significant interest due to their low-cost electron transport materials and high thermal operational stability[37–58]. Moreover, it is well known that nearly all record PCEs that LPSCs were certified by the National Renewable Energy Laboratory (NREL) were achieved in the *nip* architectures[59]. As such, *nip* architecture should be the preferred platform for high-performing TPSCs as well although their PCEs are not satisfied so far[37–58]. A key contributing factor for the unsatisfied performance of *nip*-type TPSCs is the indiscriminate adoption of functional materials from *nip*-type LPSCs, lacking tailored design for the former. For instance, *nip*-type TPSCs to date all use metal oxides (TiO_2 and SnO_2) as electron transport layers (ETL), all of which were originally used in LPSCs[37–58]. However, they are no longer the optimal choice for TPSCs as the corresponding *nip*-type TPSCs show much lower performance than *pin*-type LPSCs and even most open-circuit voltages (V_{OC}s) of reported *nip*-type TPSCs were <0.5 V, as shown in Table S1. Theoretically, such low V_{OC}s can be attributed to the mismatched band structure between the metal oxide ETLs and Sn-based perovskite layers[25]. Moreover, the presence of oxygen vacancies in metal oxides is another possible reason for the poor performance[60–63]. Therefore, it is crucial to identify the reasons of poor performance caused by metal oxides and to explore novel ETLs to enable efficient, reliable, and scalable TPSCs.

In this work, we elucidate the origin of poor photovoltaic performance in *nip*-type TPSCs and the underlying mechanism by which metal oxide ETLs influence this performance. Specifically, we demonstrate that the desorption of oxygen molecules from oxygen vacancies in TiO_2 triggers the oxidation process from Sn^{2+} to Sn^{4+} in Sn-based perovskites. Additionally, the deeper energy levels of TiO_2 ETLs result in a reduction in V_{OC}. To address these challenges, we introduce an ETL, a metal mixed-chalcogenide of $Sn(S_{0.92}Se_{0.08})_2$, into the *nip*-type TPSC. Unlike conventional metal oxide ETLs, the $Sn(S_{0.92}Se_{0.08})_2$ ETL not only circumvents the desorption of O_2 molecules but also hinders the reaction between Sn^{2+} ions within Sn-based perovskites and O_2 molecules present in air. Moreover, the $Sn(S_{0.92}Se_{0.08})_2$ ETL exhibits a shallower CBM position compared to metal oxide counterparts. Additionally, it boasts several other advantageous properties, including improved morphology, heightened conductivity, and increased electron mobility. These attributes confer upon the *nip*-type TPSC with the $Sn(S_{0.92}Se_{0.08})_2$ ETL a significantly elevated V_{OC}, increasing from 0.48 to 0.73 V, and enhancing the PCE from 6.98 to 11.78%, representing a >65% improvement. Furthermore, our ETL substantially enhances the operational stability of the *nip*-type TPSC dramatically.

Results

To explore the impact of metal oxide ETLs on *nip*-type TPSCs, our study focused on the widely used FTO/TiO_2/Sn-based perovskite/PTAA/Ag configuration. The TiO_2 ETL was deposited onto the FTO substrate using a titanium butoxide solution and subsequently annealed at 450 °C. The Sn-based perovskite $PEA_{0.15}FA_{0.85}SnI_{2.85}Br_{0.15}$ was then deposited on the TiO_2 ETL utilizing a one-step deposition approach. Supplementary Table 1 provides a summary of representative photovoltaic performance for this specific structure[37–58]. Remarkably, Supplementary Fig. 1 highlights a significant disparity between the experimental and theoretical values of the PCE and V_{OC} in *nip*-type TPSCs. We speculate that the primary reasons to such significant discrepancy can be ascribed to the presence of oxygen vacancies and deeper band positions within the TiO_2 ETLs in *nip*-type TPSCs.

Oxygen vacancy

TiO_2 is known to contain numerous oxygen vacancies (OVs) and trivalent titanium ions (Ti^{3+}), particularly at its surface[58–61]. These OVs have the propensity to absorb molecular oxygen from the atmosphere, forming a charge transfer complex (O_2^- – Ti^{4+}). Under the external stimuli, such as light or electrons, electron-hole pairs are generated, and the resulting holes in the valence band tend to recombine with O_2^-, leading to the desorption of oxygen. For the Sn-based perovskite, as the two 5 s electrons of the Sn elements without lanthanide shrinkage are highly active and easy to lose, it is very sensitive to the oxygen[33]. The desorbed oxygen accelerates the oxidation of Sn^{2+} to Sn^{4+} within the Sn-based perovskite. Therefore, this process can be expressed by two sequential steps, the desorption of oxygen from OVs in TiO_2, followed by the oxidation of Sn-based perovskites by the released oxygen, as schematically illustrated in Fig. 1a[64,65].

To validate this hyprothesis, the electron paramagnetic resonance (EPR) measurement was conducted on TiO_2 films (Fig. 1b), which is able to evidence the OVs directly. An intense unpaired electron signal at $g = 2.004$ was recorded, suggesting the existence of OVs in TiO_2 films[61,66]. Further analysis of the chemical valence states of Ti and O elements in TiO_2 films was performed using the high-resolution X-ray photoelectron spectroscopy (XPS). Fig. 1c shows the O 1*s* core-level specturm of the TiO_2 film, revealing three distinct peaks. Peaks at 530.5 and 532.1 eV are attributed to lattice oxygen and non-lattice oxygen, respectively, while the peak at 531.3 eV is indexed to OVs, corroborating the presence of OVs in TiO_2 films. Concurrently, the formation of Ti^{3+} ions was also observed (Supplementary Fig. 2). Peaks located at binding energies of 458.9 and 464.7 eV can be attributed to Ti^{4+} $2p_{3/2}$ and Ti^{4+} $2p_{1/2}$, respectively, consistent with rutile TiO_2. In addition, Ti^{3+} $2p_{3/2}$ and Ti^{3+} $2p_{1/2}$ XPS peaks at binding energies of 457.7 and 463.8 eV can be detected as well, which is the by-product of the OVs.

To confirm the negative effects of OVs in TiO_2 films on Sn-based perovskite films, XPS spectra were conducted for the Sn-based perovskite films deposited on both FTO substrates and FTO/TiO_2 films, respectively. Since the XPS measurement is surface sensitive, a low concentration (0.1 M) of precursor solution of Sn-based perovskite was used to detect the chemical state of the buried interface between the TiO_2 film and the Sn-based perovskite film. The presence of Ti 2*p* XPS peaks (Supplementary Fig. 3) confirms the validity of the XPS measurement for the buried interface. Supplementary Fig. 4 displays XPS spectra of fresh Sn-based perovskite films on FTO and FTO/TiO_2 substrates, which suggests a similar Sn^{4+}/Sn^{2+} ratio in both samples. To eliminate effects of other factors on Sn-based perovskite films, both samples were aged in the glovebox under low light conditions. Fig. 1d, e reveal XPS spectra of Sn-based perovskite films on FTO and FTO/TiO_2 substrates after aging for 14 days, respectively. Notably, the Sn^{4+}/Sn^{2+} ratio in Sn-based perovskite films on FTO substrates remained largely unchanged, while the Sn^{4+}/Sn^{2+} ratio in Sn-based perovskite films on FTO/TiO_2 films show a significant alternation. This distinct difference suggests that desorbed oxygen from TiO_2 films result in severe oxidation in Sn-based perovskites, consequently compromising the stability of *nip*-type TPSCs over time.

Band structure

In additon to OVs, the mismatched band structure between TiO_2 and the Sn-based perovskite is another contributing factor to the low performance of *nip*-type TPSCs, especially with regard to low V_{OC}. Supplementary Fig. 5 presents the ultraviolet photoelectron spectroscopy (UPS) data, illustrating the valence band maximum (VBM) onset and the secondary electron cutoff energy boundary of TiO_2 and Sn-based perovksite films. Combining their optical bandgaps derived from adsorption spectra (Supplementary Fig. 6a–d), the VBM and conduction band minimum (CBM) energies of TiO_2 and Sn-based perovksite films were calculated, as listed in Supplementary Table 2. Notably, owing to the shallow CBM of the Sn-based perovksite, the

https://doi.org/10.1038/s41467-024-53713-4

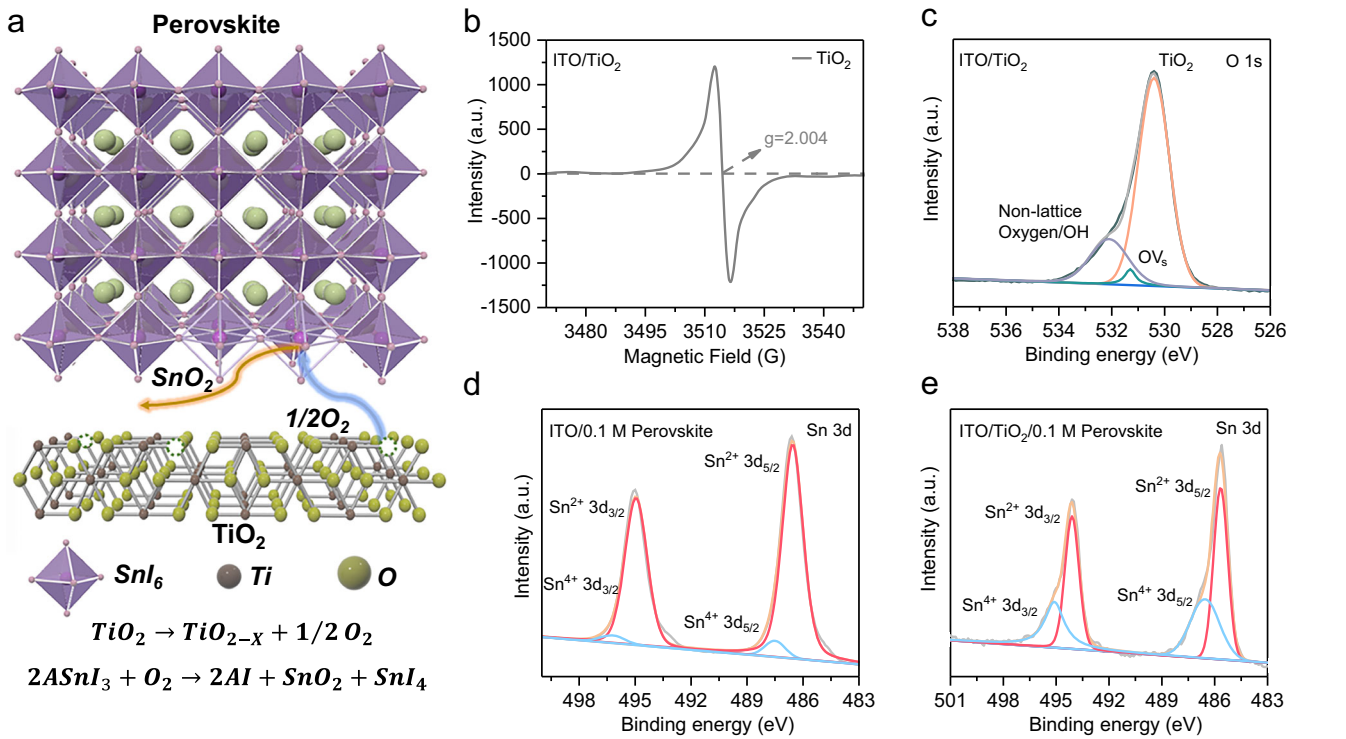

Fig. 1 | Oxygen vacancies in TiO_2 ETLs. a Schematic diagram of the buried interface between the TiO_2 ETL and Sn-based perovskite layer. Oxygen desorption from OVs in the TiO_2 ETL accelerates the oxidation of Sn^{2+} to Sn^{4+} within the Sn-based perovskite. **b** EPR spectra of the TiO_2 ETL, confirming the existence of OVs. **c** High-resolution XPS spectra in the O 1*s* region of the TiO_2 ETL, further supporting the existence of OVs. High-resolution XPS spectra of Sn-based perovskite films on (**d**) FTO and (**e**) FTO/TiO_2 substrates after aging for 14 days, respectively. This distinct difference observed suggests that desorbed oxygen from TiO_2 films leads to severe oxidation in Sn-based perovskites.

conventional TiO_2 ETL shows a substantial energy level offset due to its significantly deeper CBM position. This disparity in energy levels is crucial, as the maximum attainable V_{OC} is determined by the quasi-Fermi level splitting (Supplementary Fig. 6e). Consequently, the deeper energy level of the TiO_2 ETL results in a diminished V_{OC} value in *nip*-type TPSCs, aligning with previously reported findings (Supplementary Table 1), thus rendering it disadvantageous for *nip*-type TPSCs.

Metal mixed-chalcogenide ETL

Having identified that the root cause of the low performance of *nip*-type TPSCs lies in the presence of OVs and deeper band positions within TiO_2 ETLs, we recognize two potential strategies to address this issue. Firstly, we can aim to reduce the OVs in TiO_2 by interface engineering and simultaneously adjust the band positions of TiO_2 through composition engineering. Alternatively, we can explore the substitution of TiO_2 with other n-type semiconductors. However, despite attempts to employ individual engineering approaches in *nip*-type TPSCs, notable performance enhancements have not been consistently achieved[44,52]. Moreover, the simultaneous application of both engineering strategies to TiO_2 ETLs may yield opposite effects. Therefore, the pursuit of alternative ETLs for *nip*-type TPSCs to replace TiO_2 becomes imperative. The ideal ETL for *nip*-type TPSCs should feature several key attributes, including a favorable band structure that aligns well with Sn-based perovskites, optical transparency, a compact morphology without pinholes, and high conductivity and mobility[67–70]. Following this line of thought, we have synthesized a metal mixed-chalcogenide, $Sn(S_xSe_y)_2$, as a promising candidate for ETLs in *nip*-type TPSCs. This material was synthesized by a hydrothermal method, as depicted in Supplementary Fig. 7, with detailed synthesis procedures provided in Methods. The composition distribution and crystallization of the typical metal mixed-chalcogenide, $Sn(S_{0.92}Se_{0.08})_2$, used in this study were verified through XPS, transmission electron microscopy (TEM), and X-ray diffraction (XRD) techniques, as shown in Supplementary Figs. 8–9.

Figure 2a, b present UPS data of the VBM onset and the secondary electron cutoff energy boundary of SnS_2 and $Sn(S_{0.92}Se_{0.08})_2$ ETLs, respectively. Similar to TiO_2 ETLs, their VBM and CBM energies were computed by incorporating their optical bandgaps (Supplementary Fig. 10), as listed in Supplementary Table 2. Evidently, both SnS_2 and $Sn(S_{0.92}Se_{0.08})_2$ ETLs reveal shallower CBM positions than TiO_2 ETLs, indicating a smaller energy level offset with Sn-based perovskites and a higher V_{OC} in the corresponding *nip*-type TPSCs. Furthermore, the $Sn(S_{0.92}Se_{0.08})_2$ ETL demonstrates the shallowest CBM position, suggesting its potential as the preferred candidate for *nip*-type TPSCs as the ETL. This is the main reason that we introduced the metal mixed-chalcogenide to act as the ETL in the *nip*-type TPSC in this study. To further validate the favorable band alignment of the $Sn(S_{0.92}Se_{0.08})_2$ ETL, the Kelvin probe force microscopy (KPFM) was employed to provide reliable local surface potentials, as shown in Fig. 2c. Obviously, the surface potentials of TiO_2, SnS_2 and $Sn(S_{0.92}Se_{0.08})_2$ ETLs exhibit a consistent trend with the UPS measurements, reaffirming the suitability of the $Sn(S_{0.92}Se_{0.08})_2$ film as the optimal candidate for *nip*-type TPSCs as the ETL.

In addition to favorable band structure alignment with Sn-based perovskites, as an ideal ETL, the $Sn(S_{0.92}Se_{0.08})_2$ ETL should also possess optical transparency and a pinhole-free compact morphology. Figure 2d displays the UV-vis optical transmission spectra of the TiO_2, SnS_2 and $Sn(S_{0.92}Se_{0.08})_2$ ETLs, revealing the similar optical transparency of the $Sn(S_{0.92}Se_{0.08})_2$ ETL in the whole region. Supplementary Fig. 11a–c show top-view scanning electron microscopy (SEM) images of TiO_2, SnS_2, and $Sn(S_{0.92}Se_{0.08})_2$ ETLs. Similar to the commonly used TiO_2 ETL, SnS_2 and $Sn(S_{0.92}Se_{0.08})_2$ ETLs exhibit conformal and entire coverage on the FTO substrate, devoid of apparent pinholes. This observation is further corroborated by atomic force microscopy (AFM)

https://doi.org/10.1038/s41467-024-53713-4

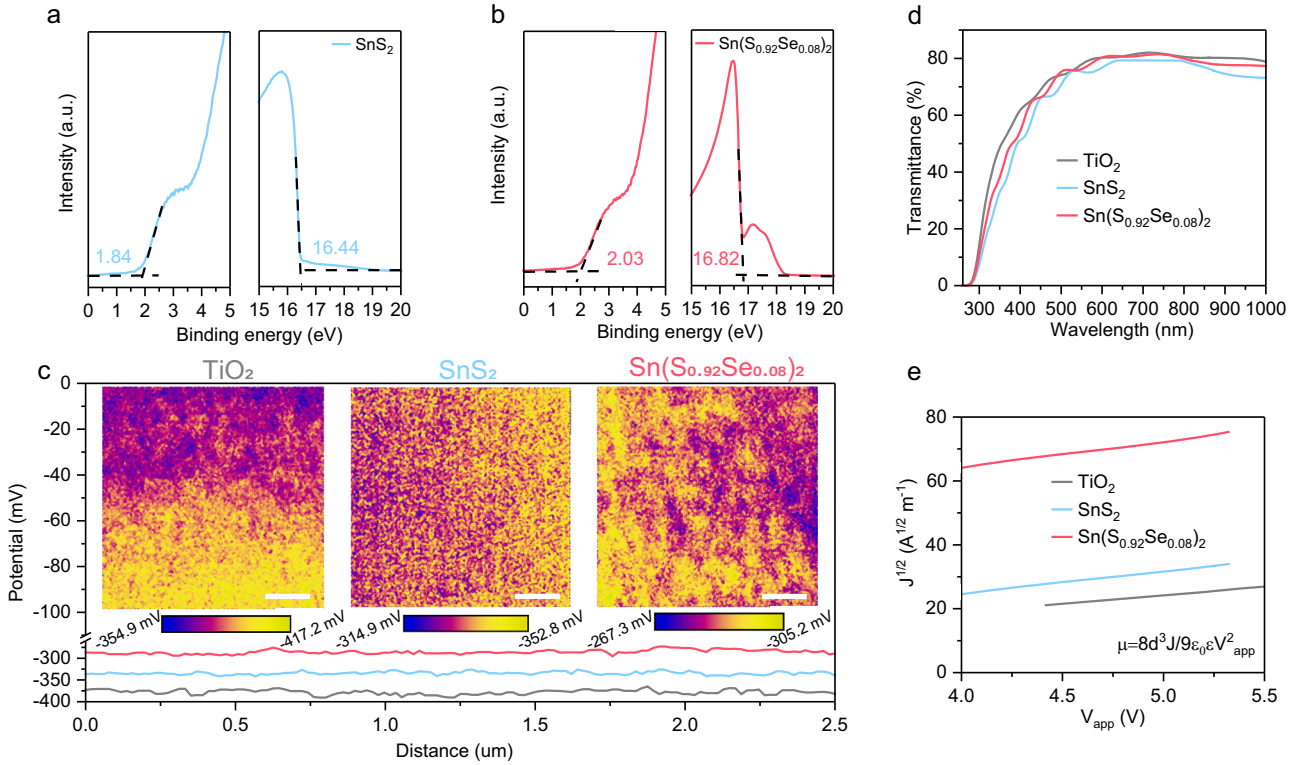

Fig. 2 | Metal chalcogenide ETLs. UPS spectra of VBM onset and photoemission cutoff energy boundary of (**a**) SnS_2 and (**b**) $Sn(S_{0.92}Se_{0.08})_2$ ETLs. The $Sn(S_{0.92}Se_{0.08})_2$ ETL shows the shallowest CBM position, highlighting its potential as the preferred ETL candidate for *nip*-type TPSCs. **c** KPFM curves and images of the TiO_2, SnS_2 and $Sn(S_{0.92}Se_{0.08})_2$ ETLs. The scalebars are 1 um. **d** UV-vis optical transmission spectra of TiO_2, SnS_2 and $Sn(S_{0.92}Se_{0.08})_2$ ETLs, revealing similar optical transparency between the $Sn(S_{0.92}Se_{0.08})_2$ ETL and the TiO_2 ETL throughout the spectrum. **e** *J-V* curves at the trap-free SCLC regime of TiO_2, SnS_2 and $Sn(S_{0.92}Se_{0.08})_2$ ETLs, fitted with the Mott-Gurney law. The results suggest that the mobility of the $Sn(S_{0.92}Se_{0.08})_2$ ETL is an order of magnitude higher than that of the TiO_2 ETL.

images of TiO_2, SnS_2, and $Sn(S_{0.92}Se_{0.08})_2$ films, as show in Supplementary Fig. 11d–f. Moreover, TiO_2, SnS_2, and $Sn(S_{0.92}Se_{0.08})_2$ films reveal consecutive decreases in root-mean-square roughness (RMS) from 20.7 to12.8–8.37 nm, suggesting that the $Sn(S_{0.92}Se_{0.08})_2$ film possesses the most compact morphology, enhancing its applicability in *nip*-type TPSCs.

Finally, the conductivity and electron mobility of the $Sn(S_{0.92}Se_{0.08})_2$ film were investigated. Supplementary Fig. 12 illustrates the current-voltage (*I-V*) curves of the devices with the FTO/ETL/Ag structure, where the ETLs are TiO_2, SnS_2, and $Sn(S_{0.92}Se_{0.08})_2$ films respectively. Corresponding conductivities were listed in Supplementary Table 3. Clearly, the $Sn(S_{0.92}Se_{0.08})_2$ ETL reveals a higher conductivity of 13.8×10^{-3} S cm^{-1} than the TiO_2 ETL (8.4×10^{-3} S cm^{-1}) and the SnS_2 ETL (12.7×10^{-3} S cm^{-1}). To quantitatively assess electron mobility, the space-charge-limited current (SCLC) measurements were performed on devices with the FTO/Ag/ETL/Ag architecture. Supplementary Fig. S13 shows the current density-voltage (*J-V*) curves of the device, which generally exhibit three regions, including an Ohmic region, a trap-filling limited region, and a trap-free SCLC regime. Figure 2e zooms in on the *J-V* curves at the trap-free SCLC regime, which represents the Mott-Gurney law and the current density (*J*) can be written by Eq. (1)[35]:

$$J = \frac{9\varepsilon\varepsilon_0 V_{app}^2 \cdot \mu}{8L^3} \quad (1)$$

where V_{app} and μ denote the voltage and mobility at the trap-free region. Accordingly, the μ for the TiO_2, SnS_2, and $Sn(S_{0.92}Se_{0.08})_2$ ETLs were listed in Supplementary Table 3. It is evident that mobilities of SnS_2 and $Sn(S_{0.92}Se_{0.08})_2$ ETLs are an order of magnitude higher than that of the TiO_2 ETL, with the $Sn(S_{0.92}Se_{0.08})_2$ ETL exhibiting the highest mobility. In short, it is demonstrated that the $Sn(S_{0.92}Se_{0.08})_2$ ETL is indeed a promising candidate for the ETL in *nip*-type TPSCs, boasting a shallow CBM position, good optical transparency, compact morphology, and superior conductivity and mobility.

Interactions between metal mixed-chalcogenide ETLs and Sn-based perovskites

After establishing the $Sn(S_{0.92}Se_{0.08})_2$ film as a promising ETL in TPSCs, it is essential to elucidate the interaction between the $Sn(S_{0.92}Se_{0.08})_2$ ETL and the Sn-based perovskite. First-principles calculations were utilized to understand this interaction. As discussed above, oxygen (O_2) molecules desorb from the OV sites in TiO_2 ETLs under external stimuli. Supplementary Figure 14a shows that the adsorption energy (E_{ads}) of O_2 molecules on the surface of Sn-based perovskite is −0.28 eV. In contrast, the E_{ads}s values of SnS_2 and $Sn(S_{0.92}Se_{0.08})_2$ ETLs are −0.30 and −0.35 eV, respectively (Supplementary Fig. 14b, c). This result indicates that SnS_2 and $Sn(S_{0.92}Se_{0.08})_2$ ETLs not only do not involve O_2 molecules desorption, but also hinder the reaction between Sn^{2+} ions in Sn-based perovskites and O_2 molecules present in air. Fig. 3a shows the calculated electron density distribution to describe the interaction between the O_2 molecule and the Sn-based perovskite. Upon O_2 adsorption on the Sn-based perovskite, the electron cloud density around Sn^{2+} noticeably transfers to the O_2 molecules, facilitating the oxidation of Sn^{2+} by O_2. However, for SnS_2 and $Sn(S_{0.92}Se_{0.08})_2$ ETLs, the electron density around Sn^{2+} was significantly increased, effectively suppressing the oxidation of Sn^{2+} (Fig. 3b, c). To quantify this interaction, the Bader charge values of O_2, SnS_2, and $Sn(S_{0.92}Se_{0.08})_2$ adsorbed on Sn-based perovskites were computed, as shown in Fig. 3a–c. The $Sn(S_{0.92}Se_{0.08})_2$ ETL on the Sn-based perovskite

https://doi.org/10.1038/s41467-024-53713-4

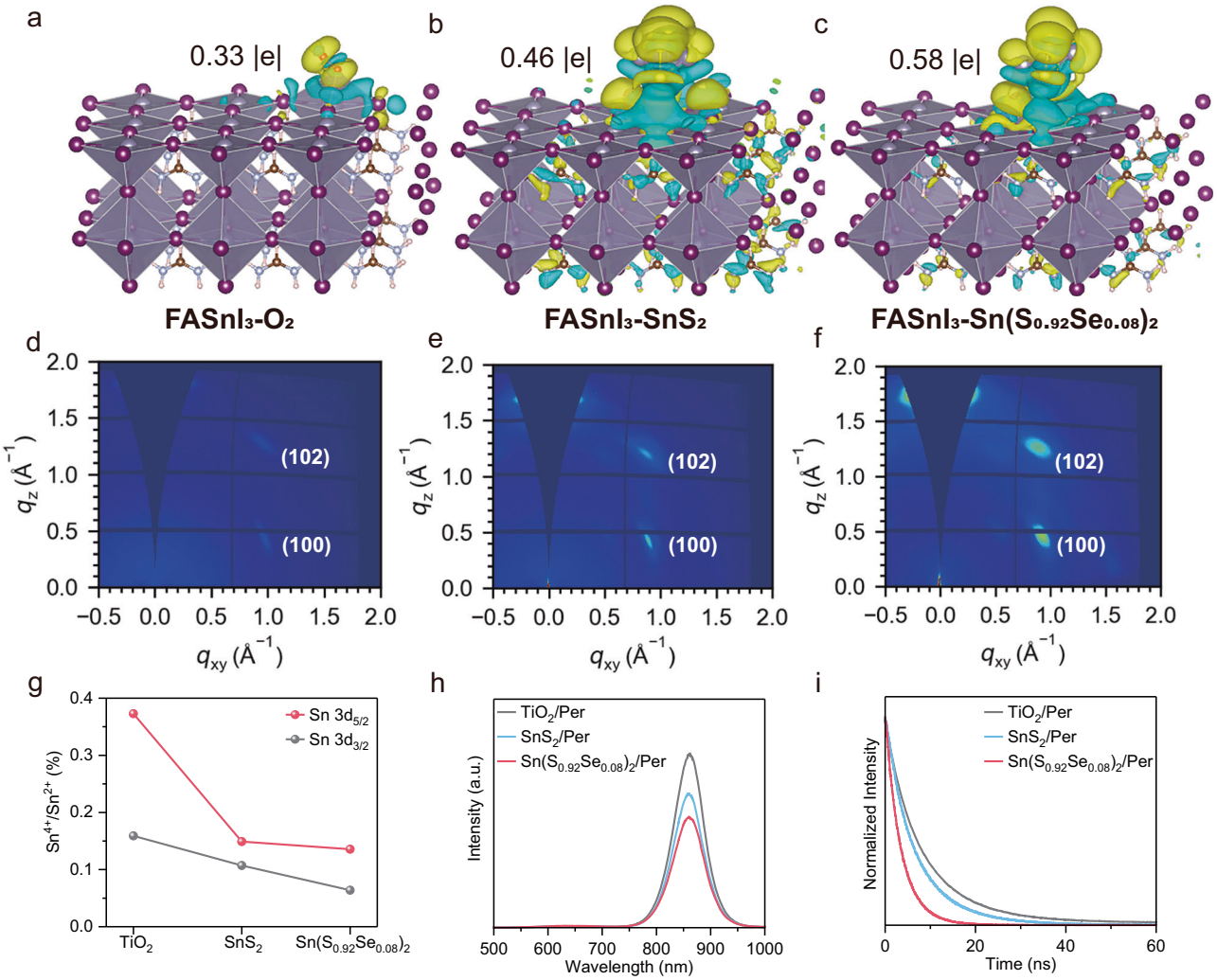

Fig. 3 | Strong interaction between metal chalcogenide ETLs and Sn-based perovskite layers. The electron density distribution of Sn-based perovskites interacting with (**a**) O_2, (**b**) SnS_2 and (**c**) $Sn(S_{0.92}Se_{0.08})_2$ molecules, indicating that the $Sn(S_{0.92}Se_{0.08})_2$ ETL not only circumvents O_2 molecules desorption, but also inhibits the reaction between Sn^{2+} ions in Sn-based perovskites and O_2 molecules present in air. GIWAXS patterns of the Sn-based perovskite films grown on (**d**) TiO_2, (**e**) SnS_2, and (**f**) $Sn(S_{0.92}Se_{0.08})_2$ ETLs respectively. These results indicate that the $Sn(S_{0.92}Se_{0.08})_2$ ETL induces the highest crystalline phase purity at the buried interface due to the strong interaction. **g** The Sn^{4+}/Sn^{2+} ratios in the Sn $3d_{5/2}$ and Sn $3d_{3/2}$ regions of the Sn-based perovskite films deposited on different ETLs, including TiO_2, SnS_2 and $Sn(S_{0.92}Se_{0.08})_2$ ETLs. The Sn-based perovskite with the $Sn(S_{0.92}Se_{0.08})_2$ ETL shows the lowest values, indicative of the strongest interaction between the two. **h** PL and (**i**) TRPL spectra of Sn-based perovskite films deposited on TiO_2, SnS_2, and $Sn(S_{0.92}Se_{0.08})_2$ ETLs, respectively. Both results suggest the fastest electron transfer in the structure of Sn-based perovskite films deposited on $Sn(S_{0.92}Se_{0.08})_2$ films.

reveals the highest Bader charge value, suggesting the strongest interaction between them.

To experimentally demonstrate the strong interaction between the $Sn(S_{0.92}Se_{0.08})_2$ ETL and the Sn-based perovskite, the interfacial effect of the $Sn(S_{0.92}Se_{0.08})_2$ ETL on the Sn-based perovskite was characterized using the grazing incidence wide-angle X-ray scattering (GIWAXS) technique. To collect buried interface information without any transfer and damage, the X-ray beam was illuminated from the back side of the Sn-based perovskite films deposited on PEN/ITO/ETL substrates, where ETLs are TiO_2, SnS_2, and $Sn(S_{0.92}Se_{0.08})_2$ films, as shown in Supplementary Fig. 15. Figure 3d–f exhibit the interface GIWAXS patterns of the Sn-based perovskite films grown on TiO_2, SnS_2, and $Sn(S_{0.92}Se_{0.08})_2$ ETLs respectively. The Sn-based perovskite films grown on SnS_2 and $Sn(S_{0.92}Se_{0.08})_2$ ETLs reveal sharper and stronger Bragg spots compared to those grown on the TiO_2 ETL, suggesting the incomplete structural transition of the Sn-based perovskite at the buried interface with the TiO_2 ETL. Moreover, the Sn-based perovskite film grown on the $Sn(S_{0.92}Se_{0.08})_2$ ETL shows sharper and stronger Bragg spots compared to those grown on the SnS_2 ETL, indicative of a higher crystalline phase purity at the corresponidng buried interface. Therefore, the use of the $Sn(S_{0.92}Se_{0.08})_2$ ETL enhances its interaction with the Sn-based perovskite, inhibits degradation of the Sn-based perovskites, and promotes the formation of a significant amount of crystallized perovskite.

The strong interaction suppresses the oxidation of Sn^{2+} in Sn-based perovskites, as demonstrated by XPS spectra after aging 14 days under low light illumination, as shown in Supplementary Fig. 16 and Fig. 3g. Compared to the Sn-based perovskite with the TiO_2 ETL, Sn-based perovskites with metal chalcogenides show significantly reduced Sn^{4+}/Sn^{2+} ratios for both Sn $3d_{5/2}$ and $3d_{3/2}$, with the Sn-based perovskite with the $Sn(S_{0.92}Se_{0.08})_2$ ETL reveals the lowest value, indicative of the strongest interaction between the two. Furthermore, the strong interaction not only suppresses the oxidation of Sn-based perovskites, but also facilitates fast electron transfer dynamics from the $Sn(S_{0.92}Se_{0.08})_2$ ETL to the Sn-based perovskite layer. Fig. 3h presents the photoluminescence (PL) spectra of the Sn-based perovskite films deposited on the TiO_2, SnS_2, and $Sn(S_{0.92}Se_{0.08})_2$ ETLs

https://doi.org/10.1038/s41467-024-53713-4

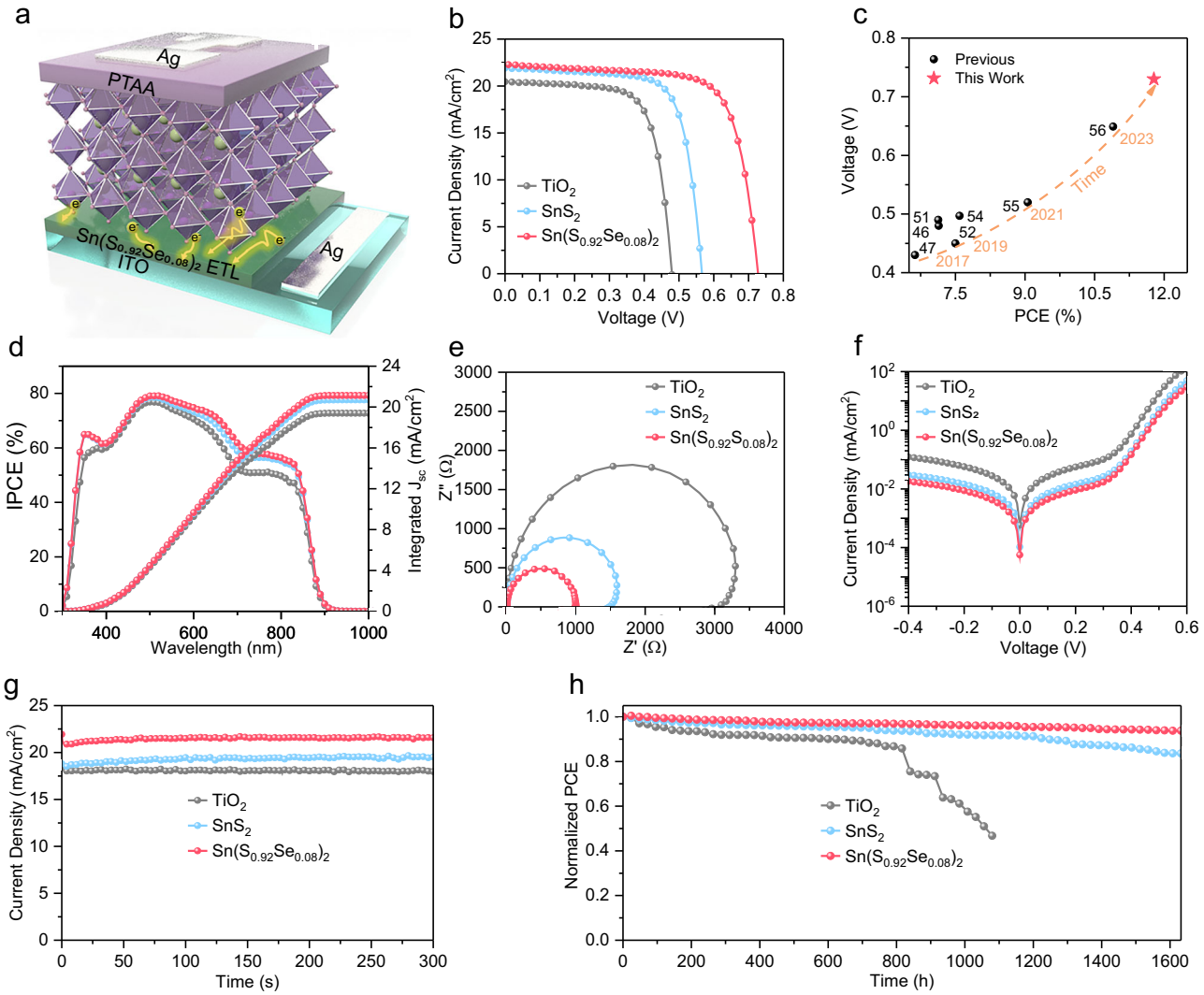

Fig. 4 | Photovoltaic performance of TPSCs with metal chalcogenide ETLs. **a** Schematic diagram of *nip*-type TPSCs with the structure of FTO/ETL/Sn-based perovskite/PTAA/Ag, utilizing TiO_2, SnS_2, and $Sn(S_{0.92}Se_{0.08})_2$ films as ETLs. **b** *J*–*V* curves of *nip*-type TPSCs with TiO_2, SnS_2 and $Sn(S_{0.92}Se_{0.08})_2$ ETLs, respectively. **c** A comparison of PCE between this work and other reported PCEs (over 6.5%) of *nip*-type TPSCs. The impressive PCE of the *nip*-type TPSC with the $Sn(S_{0.92}Se_{0.08})_2$ film significantly surpasses those of previously reported *nip*-type TPSCs with TiO_2 films. **d** EQE spectra and integrated *J*sc values of the *nip*-type TPSCs with TiO_2, SnS_2 and $Sn(S_{0.92}Se_{0.08})_2$ ETLs, respectively. **e** Nyquist plots. **f** dark *J*–*V* curves, and (**g**) stabilized power output of *nip*-type TPSCs with TiO_2, SnS_2 and $Sn(S_{0.92}Se_{0.08})_2$ ETLs respectively. These result indicate that the *nip*-type TPSC with the $Sn(S_{0.92}Se_{0.08})_2$ ETL showcases the reduced charge transfer resistance, fastest electron transport, and lowest defect density among the three types ETLs. **h** Normalized PCE of unencapsulated *nip*-type TPSCs with TiO_2, SnS_2 and $Sn(S_{0.92}Se_{0.08})_2$ ETLs for over 1600 h in an N_2 glovebox. These findings collectively support the potential of metal chalcogenide ETLs, particularly $Sn(S_{0.92}Se_{0.08})_2$, for advancing the performance and stability of *nip*-type TPSCs.

resepctively. Both the Sn-based perovskites deposited on the SnS_2 and $Sn(S_{0.92}Se_{0.08})_2$ films display lower intensities than that deposited on the TiO_2 films, indicating more efficient electron transfer from the Sn-based perovskite film to the metal chalcogenide. Meanwhile, the Sn-based perovskite film deposited on the $Sn(S_{0.92}Se_{0.08})_2$ film exhibits the lowest intensity among the three samples, which is consistent with the result that the $Sn(S_{0.92}Se_{0.08})_2$ film possesses the strongest interaction with the Sn-based perovskite. To gain more insights into effective electron transfer dynamics, time-resolved PL (TRPL) measurements were also performed to test the decay lifetime for the three samples (Fig. 3i). The corresponding TRPL lifetime was calculated by single-exponential fits to the TRPL decays, as listed in Supplementary Table 4. Clearly, the Sn-based perovskite film deposited on the $Sn(S_{0.92}Se_{0.08})_2$ film shows the shortest PL decay lifetime among the three samples. Such a short lifetime further indicates the fastest electron transfer in the structure of Sn-based perovskite films deposited on $Sn(S_{0.92}Se_{0.08})_2$ films.

Device performance

Next, we fabricated *nip*-type TPSCs with the structure of FTO/ETL/Sn-based perovskite/PTAA/Ag using TiO_2, SnS_2, and $Sn(S_{0.92}Se_{0.08})_2$ films as ETLs (Fig. 4a). Detailed information on the synthesis procedure can be found in the Method Section. Fig. 4b shows the current density-voltage (*J*–*V*) curves of the best-performing *nip*-type TPSCs with TiO_2, SnS_2, and $Sn(S_{0.92}Se_{0.08})_2$ ETLs. The corresponding photovoltaic parameters were listed in Supplementary Table 5. The *nip*-type TPSC with the TiO_2 ETL exhibits a PCE of 6.98%, with a V_{OC} of 0.48 V, a short circuit current density (J_{SC}) of 20.47 mA/cm^2, and a fill factor (FF) of 71.11%, comparable with previous reports. As anticipated, using metal chalcogenide as ETLs, all the photovoltaic parameters of *nip*-type TPSCs were significant increased. Specifically, the *nip*-type TPSC with the SnS_2 ETL shows a PCE of 9.03%, with V_{OC} = 0.57 V, J_{SC} = 21.89 mA/cm^2, and FF = 72.88%, and the *nip*-type TPSC with the $Sn(S_{0.92}Se_{0.08})_2$ ETL shows a PCE 11.78%, with V_{OC} = 0.73 V, J_{SC} = 22.28 mA/cm^2, and FF = 72.68%. An enhancement of over 65% in PCE was achieved when

the commonly used TiO_2 ETL was substituted by the $Sn(S_{0.92}Se_{0.08})_2$ ETL in *nip*-type TPSCs. Notably, we also obtained a certified PCE of 10.57% for the *nip*-type TPSC first time from Shanghai Institute of Microsystem and Information Technology (Supplementary Fig. 17). As shown in Fig. 4b, c, this substantial enhancement can primarily be ascribed to the improved V_{OC}, a consequence of the shallow CBM position in the $Sn(S_{0.92}Se_{0.08})_2$ ETL (Supplementary Table 2). Moreover, $Sn(S_{0.92}Se_{0.08})_2$ ETL also facilitates the growth of highly crystalline, vertically oriented and grain-through structures in the Sn-based perovskite film, as shown in Supplementary Figs. 18–19, which leads to a higher J_{SC} for the corresponding *nip*-type TPSC. Fig. 4c further demonstrates that the impressive PCE of the *nip*-type TPSC with the $Sn(S_{0.92}Se_{0.08})_2$ film, which significantly surpasses those of previously reported *nip*-type TPSCs with TiO_2 films. Despite this significant advance, it is imperative to further enhance the photovoltaic performance of *nip*-type TPSCs by several strategies in the future. For instance, introducing additives into the $Sn(S_{0.92}Se_{0.08})_2$ ETL could furture elevate its CBM. Additionally, applying an ultratin layer on the $Sn(S_{0.92}Se_{0.08})_2$ ETL surface may help to suppress the recombination and improve the morphology of the Sn-based perovskite layer. These approaches are crucial for further optimizing the performance of nip-type TPSCs.

The other ratios of Se/S in the metal chalcogenide of $Sn(S_xSe_y)_2$ ETLs were also investigated in *nip*-type TPSCs, as shown in Supplementary Fig. 20 and Supplementary Table 5. Increasing the Se ratio results in a higher V_{OC} due to the shallower CBM of the corresponding ETL, as show in Supplementary Fig. 21. However, this increase in Se ratio also leads to more severe nonradiative interfacial recombination within certain limits (Supplementary Fig. 22), Consequently, the TPSC with the $Sn(S_{0.92}Se_{0.08})_2$ ETL shows the highest PCE. Fig. 4d presents the incident photo-to-electric current conversion efficiency (IPCE) spectra and integrated J_{SC}s of *nip*-type TPSCs with TiO_2, SnS_2, and $Sn(S_{0.92}Se_{0.08})_2$ ETLs. The margin of error for J_{SC}s is around 5%, consistent with previous literature[71]. Such minor discrepancy can be ascribed to differences in measurement conditions (such as, the solar simulator and IPCE setup), preconditioning of samples for IPCE measurements, and variations in ion migration dynamics[72]. To verify reproducibility, 24 individual *nip*-type TPSCs with TiO_2, SnS_2, and $Sn(S_xSe_y)_2$ ETLs for each were fabricated, as shown in Supplementary Fig. 23. This result demonstrates that the PCEs of *nip*-type TPSCs with metal chalcogenide ETLs distribute over narrower ranges than that of *nip*-type TPSCs with TiO_2 ETLs, indicating high reproducibility of formers.

To delve deeper into the superior performance of the *nip*-type TPSC with the $Sn(S_{0.92}Se_{0.08})_2$ ETL, we conducted futher analysis of photovoltaic parameters. Electrochemical impedance spectroscopy (EIS) spectra were employed to probe the interface properties of *nip*-type TPSCs with TiO_2, SnS_2, and $Sn(S_{0.92}Se_{0.08})_2$ ETLs, as shown in Fig. 4e. Comparatively, the *nip*-type TPSCs with SnS_2 and $Sn(S_{0.92}Se_{0.08})_2$ ETLs reveal reduced series resistances and charge transfer resistances compared to those with TiO_2 ETLs, implying significantly enhanced electron transport between the metal chalcogenide layer and the Sn-based perovskite layer. This observation is consistent with Fig. 3h, i and the *nip*-type TPSC with the $Sn(S_{0.92}Se_{0.08})_2$ ETL reveal the lowest resistance and charge transfer resistance, and thus the fastest electron transport. Additionally, the *nip*-type TPSC with the $Sn(S_{0.92}Se_{0.08})_2$ ETL reveals the highest carrier recombination resistance, suggesting effective suppression of carrier recombination at the interface between the Sn-based perovskite layer and the $Sn(S_{0.92}Se_{0.08})_2$ ETL. This suppression can be attributed to the reduced defect density in the Sn-based perovskite film and at the interface with the $Sn(S_{0.92}Se_{0.08})_2$ ETL. To explore these defects further, we analyzed the dark *J-V* curves, as shown in Fig. 4f. Clearly, the dark J_{SC} of the *nip*-type TPSC with the $Sn(S_{0.92}Se_{0.08})_2$ ETL is one order of magnitude lower than that of the *nip*-type TPSC with the TiO_2 ETL, indicating a reduced defect density upon substituting TiO_2 with $Sn(S_{0.92}Se_{0.08})_2$ in *nip*-type TPSCs. Additionally, the plots of the V_{OC} versus incident light intensity further supported these findings (Supplementary Fig. 24). The ideality factor (n = 1.28 kT/q) for the *nip*-type TPSC with the $Sn(S_{0.92}Se_{0.08})_2$ ETL is closer to 1 kT/q and much smaller than those of *nip*-type TPSCs with the c-TiO_2 ETL (n = 1.64 kT/q) and the SnS_2 ETL (n = 1.51 kT/q), signifying improved device characteristics.

Finally, the long-term stability of *nip*-type TPSCs with TiO_2, SnS_2, and $Sn(S_{0.92}Se_{0.08})_2$ ETLs was examined under ambient conditions. Fig. 4g shows the stable power outputs at the maximum power point for the *nip*-type TPSC with the $Sn(S_{0.92}Se_{0.08})_2$ ETL, indicating its robust stability under constant illumination. Fig. 4h reveals the normalized PCE of encapsulated *nip*-type TPSCs with TiO_2, SnS_2, and $Sn(S_{0.92}Se_{0.08})_2$ ETLs as a function of aging time under ambient atmosphere. Obviously, the degradation of the three devices is significantly different. The PCE of the *nip*-type TPSCs with the TiO_2 ETL shows a rapid degradation after 912 h, which retains only 40% of its initial efficiency after 1080 h. The *nip*-type TPSCs with the SnS_2 ETL still retains >80% of its initial efficiency after 1632 h. Notably, the *nip*-type TPSC with the $Sn(S_{0.92}Se_{0.08})_2$ ETL still retains over 95% of its initial efficiency after 1632 h, which is of particular interest for practical applications. This underscores the potential of metal chalcogenide ETLs, particularly $Sn(S_{0.92}Se_{0.08})_2$, as a top candidate for achieving long-term stability in *nip*-type TPSCs, as summarized in recent stability studies (Supplementary Table 1). To comprehend this excellent stability, XRD patterns for *nip*-type TPSCs with TiO_2, SnS_2, and $Sn(S_{0.92}Se_{0.08})_2$ ETLs were tested at different aging time, as shown in Supplementary Fig. 25. The XRD patterns of Sn-based perovskites on TiO_2 ETLs exhibit an additional peak indexing to SnI_4 (PDF#06-0232) after aging for 24 days[64,65,73]. In contrast, the XRD patterns of Sn-based perovksites on the metal chalcogenide ETLs (SnS_2 and $Sn(S_{0.92}Se_{0.08})_2$) reveal the same peak even aging for 24 days. This result strongly verified that the Sn-based perovskites on TiO_2 ETLs did react with the oxygen molecules desorbed from the OV sites in TiO_2 ETL, as discussed in Fig. 3, suggesting that metal chalcogenides, especially the $Sn(S_{0.92}Se_{0.08})_2$, are promising ETL candidates for *nip-type* TPSCs with high PCE and stability.

Discussion

In conclusion, our investigation has unveiled the fundamental causes and underlying mechanisms behind the detrimental impact of metal oxide ETLs on the performance of *nip*-type TPSCs. This is primarily due to two factors: the oxygen molecules desorption from oxygen vacancies, which oxidizes Sn^{2+} to Sn^{4+} in Sn-based perovskites, and the mismatched energy levels of TiO_2 ETLs, which reduce the V_{OC}. To address these issues, we introduced an ETL, a metal mixed-chalcogenide of $Sn(S_{0.92}Se_{0.08})_2$, into the *nip*-type TPSC. Both experimental and theoretical findings demonstrate that the $Sn(S_{0.92}Se_{0.08})_2$ ETL circumvents O_2 desorption, hinders the reaction between Sn^{2+} ions and O_2 present in air, and offers a shallower CBM position, improved morphology, heightened conductivity, and increased electron mobility. Consequently, *nip*-type TPSCs with $Sn(S_{0.92}Se_{0.08})_2$ ETLs achieve a significantly elevated V_{OC}, increasing from 0.48 to 0.73 V, and an enhanced PCE, rising from 6.98 – 11.78%, representing a >65% improvement. Furthermore, the $Sn(S_{0.92}Se_{0.08})_2$ ETL substantially enhances the operational stability of *nip*-type TPSCs, retaining over 95% of their initial efficiency after 1632 h, compared to repid degradation after 912 h with TiO_2 ETLs. This study highlights the substantial potential of metal chalcogenide ETLs in advancing *nip*-type TPSC performance.

Methods

Materials

Tin (IV) chloride pentahydrate ($SnCl_4{\cdot}5H_2O$, 98%), Selenourea (CH_4N_2Se, 98%), Thioacetamide (ACS, ≥99.0%) and 2-(2-Aminoethyl)

isothiourea dihydrobromide (AET, 99%) were purchased from Aladdin. Formamidinium Iodide (FAI) was purchased from TCI. Phenethylammonium bromide (PEABr, 97%), Tin iodide (SnI_2, AnhydroBeads, 99.99%), tin fluoride (SnF_2, 99%), N, N-dimethylformamide (DMF, anhydrous, 99.8%), dimethyl sulfoxide (DMSO, anhydrous, 99.9%) and chlorobenzene (CB, anhydrous, 99.8%), were obtained from Sigma-Aldrich and used as received with no further purification. a poly (triaryl amine) semiconductor (PTAA) was purchased from Xi'an Baolaite Optoelectronics Technology Co.

Device fabrication

Synthesis of metal chalcogenide nanocrystalline ($Sn(S_xSe_y)_2$). In a typical synthesis, $SnCl_4{\cdot}5H_2O$ (1 mmol) and thioacetamide (4 mmol) were dissolved in deionized water (50 mL) under vigorously magnetic stirring. The mixed solution was stirred for 1 h until a transparent solution was formed. The as-obtained transparent solution was transferred to a Teflon-lined stainless-steel autoclave and a quartz vessel was put into Teflon-lined autoclave to contain the HCl aqueous solution (0.5 ml HCl 37 wt% aqueous solution in 5 ml DI). Then heated in an electric oven at 160 °C for 6 h. After the hydrothermal synthesis, the obtained SnS_2 powder was cleaned with distilled water and ethanol, twice. Eventually, the SnS_2 precipitation was collected and redispersed in ethanol. For the synthesis of $Sn(S_xSe_y)_2$ ($x + y = 1$), Selenourea (CH_4N_2Se) was added to the mixing solution of $SnCl_4{\cdot}5H_2O$ and thioacetamide under vigorously magnetic stirring, and the reaction steps were the same as before.

Fabrication of ETL layers. The patterned ITO glass substrates were cleaned in an ultrasonic bath for 15 min with detergent, deionized water three times, and anhydrous ethanol, sequentially. Then, the ITO glass substrates were dried and cleaned with UV-Ozone for 20 min. After that, the synthesized SnS_2 or $Sn(S_xSe_y)_2$ were spin-coated on the ITO at 2000 rpm for 30 s. The substrates heated in a tube furnace under the protection of a nitrogen atmosphere at 150°C for 30 min.

Fabrication of perovskite layers. The deposition of the Sn perovskite layers prepared in a glove box with oxygen content of 0.1 ppm nitrogen. For the perovskite precursor solution, a 0.8 M perovskite precursor comprised of PEABr, FAI, SnI_2, SnF_2 and AET with the molar ratio of 0.15:0.85:1:0.075:0.05 was added in a mixed solvent (DMSO: DMF = 1:4 v/v) heated at 70 °C for 1 h. The perovskite precursors were spin-coated on the surfaces of the ETL films at 1000 and 5000 rpm for 10 s and 30 s respectively. During the second stage, 320 µL Chlorobenzene was dropped onto the substrates. Finally, the substrates were annealed at temperature of 60 °C for 5 min and 80 °C for 10 min.

Fabrication of HTL layers. The PTAA solution (20 mg PTAA and 2.25 mg DPI-TPFB dissolved in 1 ml chlorobenzene) was spin coated on the surfaces of the perovskite layers at 2000 rpm for 30 s and then annealed at 70 °C for 10 min. Finally, a 120 nm Ag layer was deposited using the thermal evaporation system.

Characterizations

The morphologies of the films (Morphologies of ETLs) and devices were characterized by a field-emission scanning electron microscope (FESEM) (SU8010, Hitachi). X-ray diffraction pattern data for 2θ values were collected using a Bruker AXD8 Advance diffractometer with nickel filtered Cu Kα radiation (λ = 1.5406 Å). X-ray photoelectron spectroscopy (XPS) was collected using an Escalab 250Xi XPS system (Thermo Scientific). The ex(in)-situ GIWAXS experiments were carried out at beamline BL14B1 in Shanghai Synchrotron Radiation Facility (SSRF). Time-resolved photoluminescence (TRPL) spectra were achieved by a streak camera (Hamamatsu, C6860). The laser source is an amplified titanium/sapphire laser providing 800 nm 35 fs pulses at 2 kHz which is then frequency doubled for 400 nm excitation. Steady-state Photo-Luminescence (PL) spectra were measured by a FLS920 transient optical spectrometer (Edinburgh Instruments). The space-charge-limited current (SCLC) results were obtained using a Keithley 2400 source-meter unit. AFM images of perovskite films were obtained using AFM5500.

The *J–V* curves were performed using a Keithley 2400 source-meter unit under AM 1.5 G light illumination at 100 mW cm^{-2} (1 sun). (ENLITECH SS-X100R) with forward/reverse scanning modes (rate 0.01 V s^{-1}). Before testing, the light intensity was calibrated using a standard Si reference cell (ENLITECH SRC-2020-KG1-RTD). The active area is 0.04-1 cm^2. The IPCE measurement was carried out by the QE-R system (Enlitech). Impedance spectroscopic measurements were recorded by an alternating bias of 50 mV by Zennium-pro (Zahner). The corresponding spectra were fitted by Z-View software.

Computational details

Spin-polarized electronic structure calculations were performed using the plane-wave basis set approach as implemented in the Vienna ab initio simulation package (VASP)[74]. The projector augmented wave (PAW) method was used to represent the ion–core electron interactions[75]. The valence electrons were represented with a plane wave basis set with an energy cutoff of 450 eV. Electronic exchange and correlation were described with the Perdew–Burke–Ernzerhof (PBE) functional[76]. DFT-D3 method was used to treat the van der Waals interaction[77]. A 15 Å vacuum space was used to avoid interactions between surface slabs. A 2 × 2 × 1 Monkhorst–Pack scheme was used to generate the k-point grid for the modeled Pt materials[78]. The convergence criteria for the self-consistent electronic structure and geometry were set to 10^{-5} eV and 0.05 eV/Å, respectively.

Reporting summary

Further information on research design is available in the Nature Portfolio Reporting Summary linked to this article.

Data availability

The data supporting the findings of this study are provided in the main text and the Supplementary Information. Source data are provided with this paper.

References

1. Chen, H. et al. Improved charge extraction in inverted perovskite solar cells with dual-site-binding. *Science* **384**, 189–193 (2024).
2. Zhang, S. et al. Minimizing buried interfacial defects for efficient inverted perovskite solar cells. *Science* **380**, 404–409 (2023).
3. Park, J. et al. Controlled growth of perovskite layers with volatile alkylammonium chlorides. *Nature* **616**, 724–730 (2023).
4. Liang, Z. et al. Homogenizing out-of-plane cation composition in perovskite solar cells. *Nature* **624**, 560–563 (2023).
5. Min, H. et al. Perovskite solar cells with atomically coherent interlayers on SnO_2 electrodes. *Nature* **598**, 444–450 (2021).
6. Jiang, Q. et al. Surface passivation of perovskite film for efficient solar cells. *Nat. Photon.* **13**, 460–466 (2019).
7. Jung, E. H. et al. Efficient, stable and scalable perovskite solar cells using poly(3-hexylthiophene). *Nature* **567**, 511–515 (2019).
8. Yoo, J. J. et al. Efficient perovskite solar cells via improved carrier management. *Nature* **590**, 587–593 (2021).
9. Zhou, H. et al. Interface engineering of highly efficient perovskite solar cells. *Science* **345**, 542–546 (2014).
10. Yang, T. et al. One-stone-for-two-birds strategy to attain beyond 25% perovskite solar cells. *Nat. Commun.* **14**, 839 (2023).
11. Warby, J. et al. Understanding performance limiting interfacial recombination in pin perovskite solar cells. *Adv. Energy Mater.* **12**, 2103567 (2022).
12. Stolterfoht, M. et al. Visualization and suppression of interfacial recombination for high-efficiency large-area pin perovskite solar cells. *Nat. Energy* **3**, 847–854 (2018).

13. Chen, B. et al. Passivation of the buried interface via preferential crystallization of 2D perovskite on metal oxide transport layers. *Adv. Mater.* **33**, e2103394 (2021).
14. Stolterfoht, M. et al. The impact of energy alignment and interfacial recombination on the internal and external open-circuit voltage of perovskite solar cells. *Energy Environ. Sci.* **12**, 2778–2788 (2019).
15. Futscher, M. H. et al. Defect spectroscopy in halide perovskites is dominated by ionic rather than electronic defects. *ACS Energy Lett.* **7**, 140–144 (2022).
16. McGott, D. L. et al. 3D/2D passivation as a secret to success for polycrystalline thin-film solar cells. *Joule* **5**, 1057–1073 (2021).
17. Tao, S. et al. Absolute energy level positions in tin- and lead-based halide perovskites. *Nat. Commun.* **10**, 2560 (2019).
18. Li, X. et al. On-device lead sequestration for perovskite solar cells. *Nature* **578**, 555–558 (2020).
19. Wu, T. et al. Graphene-like conjugated molecule as hole-selective contact for operationally stable inverted perovskite solar cells and modules. *Adv. Mater.* **35**, 2300169 (2023).
20. Bu, T. et al. Modulating crystal growth of formamidinium–caesium perovskites for over 200 cm^2 photovoltaic sub-modules. *Nat. Energy* **7**, 528 (2022).
21. Tong, G. et al. Scalable fabrication of >90 cm^2 perovskite solar modules with >1000 h operational stability based on the intermediate phase strategy. *Adv. Energy Mater.* **11**, 2003712 (2021).
22. Li, G. et al. Biotoxicity of halide perovskites in mice. *Adv. Mater.* **36**, 2306860 (2024).
23. Jiang, X. et al. One-step synthesis of SnI_2·$(DMSO)_x$ adducts for high-performance tin perovskite solar cells. *J. Am. Chem. Soc.* **143**, 10970–10976 (2021).
24. Liu, J. et al. Lead-free solar cells based on tin halide perovskite films with high coverage and improved aggregation. *Angew. Chem. Int. Ed.* **130**, 13405–13409 (2018).
25. Jiang, X. et al. Ultra-high open-circuit voltage of tin perovskite solar cells via an electron transporting layer design. *Nat. Commun.* **11**, 1245 (2020).
26. Wang, M. et al. Lead-free perovskite materials for solar cells. *Nano Micro Lett.* **13**, 1–36 (2021).
27. Yue, S. et al. Synthesis, characterization, and stability studies of Ge-based perovskites of controllable mixed cation composition, produced with an ambient surfactant-free approach. *ACS Omega* **4**, 18219–18233 (2019).
28. Jiang, F. et al. Chlorine-incorporation-induced formation of the layered phase for antimony-based Lead-free perovskite solar cells. *J. Am. Chem. Soc.* **140**, 1019–1027 (2018).
29. Park, B. W. et al. Bismuth based hybrid perovskites $A_3Bi_2I_9$ (a: methylammonium or cesium) for solar cell application. *Adv. Mater.* **27**, 6806–6813 (2015).
30. Nie, R. et al. Mixed sulfur and iodide-based lead-free perovskite solar cells. *J. Am. Chem. Soc.* **140**, 872–875 (2018).
31. Nie, R. et al. Efficient and stable antimony selenoiodide solar cells. *Adv. Sci.* **8**, 2003172 (2021).
32. Chen, J. et al. Efficient tin-based perovskite solar cells with trans-isomeric fulleropyrrolidine additives. *Nat. Photon.* **18**, 464–470 (2024).
33. Li, T. et al. Functional layers in efficient and stable inverted tin-based perovskite solar cells. *Joule* **7**, 1966–1991 (2023).
34. Zhou, X. et al. Additive engineering with 2, 8-dibromo-dibenzothiophene-S, S-dioxide enabled tin-based perovskite solar cells with 14.98% power conversion efficiency. *Energy Environ. Sci.* **17**, 2837–2844 (2024).
35. Li, T. et al. Alleviating the crystallization dynamics and suppressing the oxidation process for tin-based perovskite solar cells with fill factors exceeding 80 percent. *Adv. Funct. Mater.* **33**, 2308457 (2023).
36. Shi, Y. et al. Interfacial dipoles boost open-circuit voltage of tin halide perovskite solar cells. *ACS Energy Lett.* **9**, 1895–1897 (2024).
37. Noel, N. K. et al. Lead-free organic-inorganic tin halide perovskites for photovoltaic applications. *Energy Environ. Sci.* **7**, 3061–3068 (2014).
38. Hao, F. et al. Lead-free solid-state organic-inorganic halide perovskite solar cells. *Nat. Photon.* **8**, 489–494 (2014).
39. Islam, B. et al. Simulating the effect of inserting Sb_2S_3 as hole transport layer on SnS-based thin-film solar cells. *J. Electron* **53**, 4726–4739 (2024).
40. Kumar, M. H. et al. Lead-free halide perovskite solar cells with high photocurrents realized through vacancy modulation. *Adv. Mater.* **26**, 7122–7127 (2014).
41. Koh, T. M. et al. Formamidinium tin-based perovskite with low Eg for photovoltaic applications. *J. Mater. Chem. A.* **3**, 14996–15000 (2015).
42. Hao, F. et al. Solvent-mediated crystallization of $CH_3NH_3SnI_3$ films for heterojunction depleted perovskite solar cells. *J. Am. Chem. Soc.* **137**, 11445–11452 (2015).
43. Lee, S. J. et al. Fabrication of efficient formamidinium tin iodide perovskite solar cells through SnF_2–pyrazine complex. *J. Am. Chem. Soc.* **138**, 3974–3977 (2016).
44. Li, W. et al. Addictive-assisted construction of all-inorganic $CsSnIBr_2$ mesoscopic perovskite solar cells with superior thermal stability up to 473 K. *J. Mater. Chem. A.* **4**, 17104–17110 (2016).
45. Mahmud, J. et al. Design and analysis of a $SnS_2/WS_2/V_2O_5$ double-heterojunction toward high-performance photovoltaics. *Energy Adv.* **2**, 1843–1858 (2023).
46. Song, T.-B. et al. Importance of reducing vapor atmosphere in the fabrication of tin-based perovskite solar cells. *J. Am. Chem. Soc.* **139**, 836–842 (2017).
47. Cao, D. H. et al. Thin films and solar cells based on semiconducting two-dimensional Ruddlesden–Popper $(CH_3(CH_2)_3NH_3)_2(CH_3NH_3)_{n-1}SnnI_{3n+1}$ perovskites. *ACS Energy Lett.* **2**, 982–990 (2017).
48. Ke, W. et al. Enhanced photovoltaic performance and stability with a new type of hollow 3D perovskite {en}$FASnI_3$. *Sci. Adv.* **3**, e1701293 (2017).
49. Ke, W. et al. Efficient lead-free solar cells based on hollow {en}$MASnI_3$ perovskites. *J. Am. Chem. Soc.* **139**, 14800–14806 (2017).
50. Xiao, M. et al. Tin-based perovskite with improved coverage and crystallinity through tin-fluoride-assisted heterogeneous nucleation. *Adv. Opt. Mater.* **6**, 1700615 (2018).
51. Tsai, C.-M. et al. Control of crystal structures and optical properties with hybrid formamidinium and 2-hydroxyethylammonium cations for mesoscopic carbon-electrode tin-based perovskite solar cells. *ACS Energy Lett.* **3**, 2077–2085 (2018).
52. Chen, M. et al. Lead-free Dion–Jacobson tin halide perovskites for photovoltaics. *ACS Energy Lett.* **4**, 276–277 (2019).
53. Li, F. et al. A cation-exchange approach for the fabrication of efficient methylammonium tin iodide perovskite solar cells. *Angew. Chem. Int. Ed.* **58**, 6688–6692 (2019).
54. Vegiraju, S. et al. Benzodithiophene hole-transporting materials for efficient tin-based perovskite solar cells. *Adv. Funct. Mater.* **29**, 1905393 (2019).
55. Li, F. et al. Effects of alkyl chain length on crystal growth and oxidation process of two-dimensional tin halide perovskites. *ACS Energy Lett.* **5**, 1422–1429 (2020).
56. Tao, Y. et al. Ambient-air-stable lead-free $CsSnI_3$ solar cells with greater than 7.5% efficiency. *J. Am. Chem. Soc.* **143**, 4319–4328 (2021).
57. Hu, M. et al. Regulating the surface passivation and residual strain in pure tin perovskite films. *ACS Energy Lett.* **6**, 3555–3562 (2021).

58. Hu, M. et al. Highly stable n–i–p structured formamidinium tin triiodide solar cells through the stabilization of surface Sn^{2+} cations. *Adv. Funct. Mater.* **33**, 2300693 (2023).
59. NREL Transforming Energy. *Best Rsearch-Cell Efficiency Chart*. https://www.nrel.gov/pv/cell-efficiency.html (2024).
60. Luo, M. Q. et al. Precisely dominating oxygen vacancy of Magneli phase titanium suboxides to efficiently remove quinolone antibiotics under visible light. *Sep. Purif.* **341**, 126626 (2024).
61. Feng, N. et al. Efficient and selective photocatalytic CH_4 conversion to CH_3OH with O_2 by controlling overoxidation on TiO_2. *Nat. Commun.* **12**, 4652 (2021).
62. Wang, Y. et al. Fluorine-induced oxygen vacancies on TiO_2 nanosheets for photocatalytic indoor V_{OC}s degradation. *Appl. Catal. B. Environ.* **316**, 121610 (2022).
63. Wei, Z.-W. et al. Reversed charge transfer and enhanced hydrogen spill over in platinum nanoclusters anchored on titanium oxide with rich oxygen vacancies boost hydrogen evolution reaction. *Angew. Chem. Int. Ed.* **60**, 16622–16627 (2021).
64. Leijtens, T. et al. Mechanism of tin oxidation and stabilization by lead substitution in tin halide perovskites. *ACS Energy Lett.* **2**, 2159–2165 (2017).
65. Zhang, Z. et al. Mechanistic understanding of oxidation of tin-based perovskite solar cells and mitigation strategies. *Angew. Chem. Int. Ed.* **62**, e202308093 (2023).
66. Gan, Q. et al. Defect-assisted selective surface phosphorus doping to enhance rate capability of titanium dioxide for sodium ion batteries. *ACS Nano.* **13**, 9247–9258 (2019).
67. Park, S. et al. Advances in SnO_2 for efficient and stable n–i–p perovskite solar cells. *Adv. Mater.* **34**, 2110438 (2022).
68. Jiang, Q. et al. Enhanced electron extraction using SnO_2 for high-efficiency planar-structure $HC(NH_2)_2PbI_3$-based perovskite solar cells. *Nat. Energy* **2**, 16177 (2017).
69. Wang, L. et al. Strain modulation for light-stable n–i–p perovskite/silicon tandem solar cells. *Adv. Mater.* **34**, 2201315 (2022).
70. Kumar, N. et al. A review on perovskite solar cells (PSCs), materials and applications. *J. Mater.* **7**, 940–956 (2021).
71. Liu, C. et al. Two-dimensional perovskitoids enhance stability in perovskite solar cells. *Nature* https://doi.org/10.1038/s41586-024-07764-8 (2024).
72. Michael, S. et al. Current density mismatch in perovskite solar cells. *ACS Energy Lett.* **5**, 2886–2888 (2020).
73. Liang, H. et al. High color purity lead-free perovskite light-emitting diodes via Sn stabilization. *Adv. Sci.* **7**, 1903213 (2020).
74. Kresse, G. et al. Efficiency of ab-initio total energy calculations for metals and semiconductors using a plane-wave basis set. *Comput. Mater. Sci.* **6**, 15–50 (1996).
75. Kresse, G. et al. From ultrasoft pseudopotentials to the projector augmented-wave method. *Phys. Rev. B.* **59**, 1758–1775 (1999).
76. Perdew, J. P. et al. Generalized gradient approximation made simple. *Phys. Rev. Lett.* **77**, 3865–3868 (1996). **1996**.
77. Grimme, S. et al. A consistent and accurate ab initio parametrization of density functional dispersion correction (DFT-D) for the 94 elements H-Pu. *J. Chem. Phys.* **132**, 154104 (2010).
78. Chadi, D. J. et al. Special points for brillouin-zone integrations. *Phys. Rev. B.* **16**, 1746–1747 (1977).

Acknowledgements

J.L. acknowledges the funding support from the National Natural Science Foundation of China (52102219 and 52471197) and the Natural Science Foundation of Shanghai (21ZR1404900).

Author contributions

T.L. and B.L. contributed equally to this work. J.L. conceived the idea, designed the experiments, and supervised the research. T.L. fabricated and characterized the devices. B.L. carried out the synthesis experiment. Y.Y. contributed to the GIWAXS test. Z.Z. contributed to the EPR spectra. P.W. and Z.J. contributed to IPCE spectra. L.D. carried out the EIS experiment. Y.Z. and Q.Z. supported this work. All authors analyzed and discussed the results. T.L. wrote the draft and J.L. reviewed and edited the manuscript.

Competing interests

The authors declare no competing interests.

Additional information

Supplementary information The online version contains supplementary material available at https://doi.org/10.1038/s41467-024-53713-4.

Correspondence and requests for materials should be addressed to Jia Liang.

Peer review information *Nature Communications* thanks the anonymous reviewers for their contribution to the peer review of this work. A peer review file is available.